Journal of
Applied Crystallography
ISSN 0021-8898

Received 14 August 2006
Accepted 13 January 2007

Low-resolution models for nucleic acids from small-angle X-ray scattering with applications to electrostatic modeling

Jan Lipfert,[a] Vincent B. Chu,[b] Yu Bai,[c] Daniel Herschlag[d] and Sebastian Doniach[a,b,c,e]*

[a]Department of Physics, Stanford University, Stanford, CA 94305, USA, [b]Department of Applied Physics, Stanford University, Stanford, CA 94305, USA, [c]Biophysics Program, Stanford University, Stanford, CA 94305, USA, [d]Department of Biochemistry, Stanford University, Stanford, CA 94305, USA, and [e]Stanford Synchrotron Radiation Laboratory, Stanford University, Stanford, CA 94305, USA. Correspondence e-mail: doniach@drizzle.stanford.edu

Several algorithms are available to reconstruct low-resolution electron density maps of biological macromolecules from small-angle solution scattering data. These algorithms have been extensively applied to proteins and protein complexes. Here, we demonstrate their applicability to nucleic acids by reconstructing a set of RNA and DNA molecules of known three-dimensional structure from their small-angle X-ray scattering profiles. The overall size and shape of the molecules get reproduced well in all tested cases. Furthermore, we show that the generated bead models can be used as inputs for electrostatic calculations. The number of ions bound under different solution conditions computed from numerical solutions of the Poisson–Boltzmann equation for bead models agrees very well with results of calculations on all atom models derived from crystallography. The predictions from Poisson–Boltzmann theory also agree generally well with experimentally determined ion binding numbers.

© 2007 International Union of Crystallography
Printed in Singapore – all rights reserved

1. Introduction

Many RNAs, like proteins, can fold into intricate three-dimensional shapes and carry out complex physiological functions in the cell, such as chemical catalysis (Gesteland *et al.*, 2006) and gene regulation (Mandal & Breaker, 2004). Despite their growing importance, high-resolution structure determination by crystallography or nuclear magnetic resonance (NMR) spectroscopy remains a formidable challenge for RNAs. Furthermore, to understand RNA or protein folding and conformational changes, it is necessary to consider unfolded and partially folded ensembles of structures, for which high-resolution structures are difficult or impossible to obtain.

Small-angle X-ray scattering (SAXS) can provide low-resolution structural information and monitor conformational changes under different solution conditions (Doniach, 2001; Svergun & Koch, 2003) and has provided important insights into counterion-dependent RNA folding (Russell *et al.*, 2000; Fang *et al.*, 2000; Fang *et al.*, 2001; Russell *et al.*, 2002; Das *et al.*, 2003; Takamoto *et al.*, 2004; Woodson, 2005).

Several algorithms have been developed to obtain low-resolution three-dimensional density maps from SAXS profiles (Chacón *et al.*, 1998; Svergun, 1999; Walther *et al.*, 2000; Svergun *et al.*, 2001). Their common strategy is to place uniform point scatterers or 'beads' such that their scattering pattern best matches the experimentally measured SAXS profile. These low-resolution reconstruction methods have been extensively tested on and applied to proteins and protein complexes. Here, we investigate their applicability to nucleic acids. We reconstruct low-resolution models from SAXS data of several test molecules with known high-resolution structures. Our results show that bead reconstruction algorithms can reproduce the shape and overall geometry of nucleic acid molecules from solution scattering data.

In addition, we present an application of low-resolution bead models derived from solution scattering data to electrostatic calculations. As nucleic acids are highly negatively charged, electrostatics and the associated counterion cloud play an important role in their function and stability. In particular, RNA molecules require the presence of divalent ions (or high concentrations of monovalent ions in some cases) to fold into the three-dimensional shapes that allow them to carry out their physiological function (Draper *et al.*, 2005; Takamoto *et al.*, 2004; Woodson, 2005). Electrostatic calculations, such as Poisson–Boltzmann (PB) theory or Monte Carlo simulations have been used successfully to model the thermodynamics of ion binding to nucleic acids. The RNA or DNA molecules have been represented in these calculations either using very simplified geometries (cylinders, spheres) (Misra & Draper, 1999), or employing all atom models derived from crystallography or NMR spectroscopy (Misra & Draper, 2000).

Here we use bead model representations of the macromolecule as an input to PB calculations. This approach provides higher resolution than simple geometric models, such as spheres or cylinders, while being applicable to molecules or molecular conformations for which no atomic resolution structure is available.

2. Materials and methods

2.1. Model systems

We employed yeast $tRNA^{Phe}$, a 24 bp B-DNA duplex, and the P4P6 domain of the *Tetrahymena* group I intron as model systems.

The structures of yeast $tRNA^{Phe}$ and of the P4P6 domain were obtained by crystallography [PDB accession codes 1TRA (Westhof & Sundaralingham, 1986) and 1GID (Cate *et al.*, 1996), respectively]. The structure of a standard B-form DNA duplex was generated using the *3DNA* package (available online at http://rutchem.rutgers.edu/~xiangjun/3DNA/).

SAXS profiles for the 24 bp DNA duplex and for the P4P6 domain were measured using sample preparation procedures and a measurement set-up as described in the literature (Bai *et al.* 2005; Lipfert *et al.*, 2006; Takamoto *et al.*, 2004). The scattering data for yeast $tRNA^{Phe}$ were simulated from the crystal structure coordinates (Westhof & Sundaralingham, 1986) using the *CRYSOL* (Svergun *et al.*, 1995) program with default settings. *CRYSOL* does not consider the effect of the counterion cloud associated with the RNA. However, the good agreement between the R_g (radius of gyration) value of 23.5 Å computed by *CRYSOL* and the value measured experimentally by Sosnick and coworkers (Fang *et al.*, 2000) of 23.5 ± 0.5 Å suggests that ion scattering appears to have only a small effect on the scattering pattern in this case. We ran reconstructions using the unmodified *CRYSOL* scattering profile, as well as reconstructions for profiles with added random noise with a magnitude of 1 or 2% of the forward scattering intensity, respectively (which corresponds to noise levels similar to, or higher than, those of typical synchrotron radiation measurements). Unless otherwise noted, the results for the simulated data without added noise are presented.

2.2. Bead reconstructions

The *DAMMIN* (Svergun, 1999) program was used to construct three-dimensional models that fit the scattering data. *DAMMIN* represents the macromolecule as a set of identical point scatterers or 'beads' and uses a simulated annealing protocol to update the bead positions. Ten independent runs were performed for each scattering profile in the 'slow' mode. The program was run using default parameters and no symmetry assumptions. Each reconstruction took 9–10 h of CPU time on a 3.06 GHz Xeon workstation. The models resulting from independent runs were superimposed using the *SUPCOMB* program, which performs an initial alignment of structures based on their axes of inertia followed by minimization of the normalized spatial discrepancy (NSD) (Kozin & Svergun, 2001). The NSD has the property that it is zero for identical objects and larger than 1 for objects that systematically differ from one another. Structures with pairwise NSD values between zero and one are classified as structurally similar. The aligned structures were averaged and 'filtered' to create consensus models using the *DAMAVER* (Volkov & Svergun, 2003) program. For visualization, the reconstructed bead models were converted to electron density maps using the *SITUS* (Wriggers *et al.*, 1999; Wriggers & Chacón, 2001) program.

2.3. Ion binding measurements

Mg^{2+} ion binding to yeast $tRNA^{Phe}$ data was taken from Rialdi *et al.* (1972), who measured ion binding calorimetrically, and from Römer & Hach (1975), who used the fluorescence indicator 8-hydroxylquinoline 5-sulfonic acid (HQS) to monitor Mg^{2+} association.

Binding of Mg^{2+} ions in a 2 *M* NaCl background to P4P6 and to a P4P6 mutant that does not form the 'metal ion core' was measured using atomic emission spectroscopy (AES) and the fluorescence indicator HQS. The measurements and sample preparation are described in Das *et al.* (2005).

Comprehensive ion binding data to a 24 bp DNA duplex were measured by AES for a range of mono- and divalent ions. The methods and results are discussed in detail in Bai *et al.* (2007).

2.4. Poisson–Boltzmann calculations

We used the *APBS* program to numerically solve the PB equation (Baker *et al.*, 2001). Our simulations employed a multi-grid focusing procedure and used a grid spacing of 1.4 Å for the fine grid. The fine-grid sizes were 192 × 192 × 576 Å for the 24 bp DNA duplex, 266 × 231 × 346 Å for $tRNA^{Phe}$ and 308 × 247 × 322 Å for P4P6. Control calculations with different grid spacings (1–2 Å) and box sizes (× 0.5–2) gave virtually identical results (data not shown). The aqueous solvent was represented as a uniform dielectric with $\varepsilon = 78.54$, the dielectric constant of water. The interior of the macromolecule was assigned a dielectric constant of $\varepsilon = 2$. Dirichlet boundary conditions were set using the multiple Debye–Hückel functionality of *APBS*. Test calculations with the potential at the outer boundary set to zero produced virtually identical results (data not shown).

For each of the three test molecules, we ran two different sets of PB calculations. For the 'PDB model' simulations, the fixed charge density of the macromolecule was determined using the atomic positions from the crystal structures and assigned partial charges and atomic radii according to the CHARMM parameter set (MacKerell, 1998) using the *pdb2pqr* utility of *APBS*. The solvent and ion-accessible volume was determined from the atomic radii augmented by a 1.4 Å layer, which corresponds to the approximate radius of water. For the 'bead model' calculations, the macromolecule is represented by the bead positions. The 'atomic' radii were set to half the lattice spacing of the bead model and the water layer radius is the same as for the atomic resolution models, such that the interior of the molecule comprises the region filled with beads. As there is no direct correspondence between beads and atoms or residues of the molecule, the total charge of the molecule, Q_{tot} was divided equally between all beads, *i.e.* each of the N_b beads carries a charge $Q_b = Q_{tot}/N_b$. From the solutions of the PB equation the number of excess ions of each ion species bound to the macromolecule was computed as described in Misra & Draper (2000).

3. Results

3.1. Low-resolution reconstructions

We have reconstructed low-resolution density maps from SAXS data for yeast $tRNA^{Phe}$, a 24 bp B-DNA duplex and the P4P6 domain of the *Tetrahymena* group I intron (see Materials and methods). Figs. 1, 3 and 5 show the experimental scattering profiles $I\exp(q)$ (symbols) along with the reconstructed scattering profiles $I_{beads}(q)$ (solid lines) as a function of the modulus of the scattering vector, q [$q = 4\pi\sin(\theta)/\lambda$, where 2θ is the total scattering angle and λ is the X-ray wavelength]. The insets show the relative errors $[I_{exp}(q) - I_{beads}(q)]/I_{exp}(q) \times 100\%$.

For the $tRNA^{Phe}$, Fig. 1 shows the results using the 'experimental' data simulated from the atomic resolution structure without added noise. The relative error is below one percent. Results for the data with added noise are discussed below. For the 24 bp duplex and the P4P6 domain the relative error tends to be larger at higher scattering angles, which reflects the lower experimental signal-to-noise ratio in this region. Overall, the reconstructed profiles agree very well with the experimental data.

However, the correspondence between structure and scattering profile is not unique. To test the reproducibility and consistency of the reconstructions, we compare ten independent *DAMMIN* runs for the

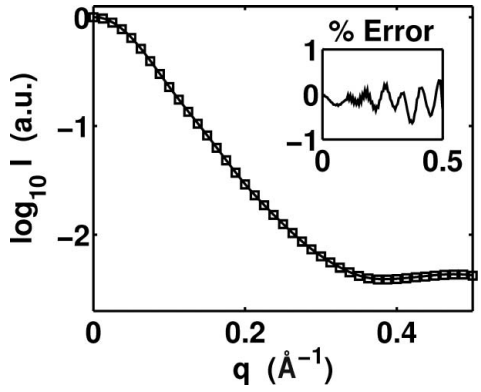

Figure 1
SAXS profiles for yeast $tRNA^{Phe}$. 'Experimental' profile (main graph, squares) simulated from the atomic coordinates using *CRYSOL* (Svergun *et al.*, 1995) and scattering profile of a representative bead reconstruction (main graph, solid line). The inset shows the relative error, defined as $[I_{exp}(q) - I_{beads}(q)]/I_{exp}(q) \times 100\%$.

same scattering profile, using the pairwise NSD criterion (see Materials and methods). The average pairwise NSD values (Table 1) are significantly less than one for all test molecules, indicating that the reconstruction algorithm is stable and converges onto similar structures in repeat runs. Finally, we compare the reconstructed bead models with the atomic resolution structures. The best superposition of the filtered 'consensus' models (see Materials and methods) with the PDB structures was determined using the *SUPCOMB* (Kozin & Svergun, 2001) program. Figs. 2, 4, and 6 show the bead models rendered as smooth transparent surfaces and the PDB models as black stick representations. The overall shape and size of the molecules get reproduced well. Overlap scores as defined by Walther *et al.* (2000) between bead models and PDB structures are presented in Table 1.

For $tRNA^{Phe}$ the characteristic L-shape is evident in the reconstruction (Fig. 2). However, the protruding single stranded region shown at the bottom of Fig. 2 is only reproduced incompletely in the reconstruction. Reconstructions using the scattering profiles with added noise gave results similar to those presented in Fig. 2. In particular, the models generated from the 'noisy' data give R_g values

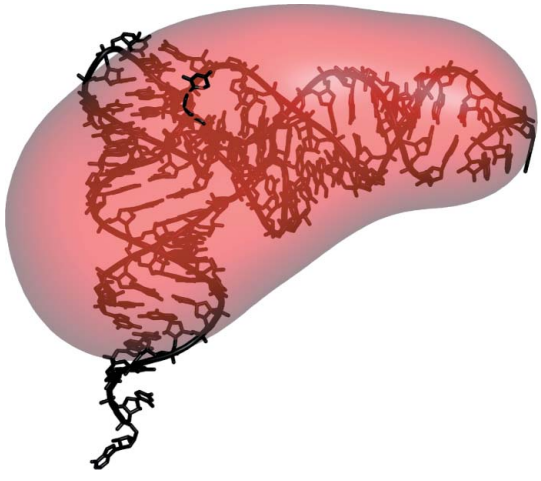

Figure 2
Atomic resolution structure of yeast $tRNA^{Phe}$ (PDB accession code 1TRA, rendered as black sticks) and reconstructed density (red transparent surface). The reconstructed density was generated from the filtered consensus bead model by smoothing with a Gaussian kernel (see Materials and methods). Molecular graphics were prepared using *PyMOL* (DeLano, 2002).

Table 1
Test molecules and overview over reconstruction results.

Experimental radii of gyration R_g (Å) were determined from Guinier analysis (Guinier, 1939) of the measured scattering profiles. The value for yeast $tRNA^{Phe}$ was taken from Fang *et al.* (2000). The 'PDB' values of R_g were computed from the PDB structures using *CRYSOL* with default parameters. The R_g values from bead models represent the mean and standard deviation from ten independent reconstructions. ⟨NSD⟩ gives the mean and standard deviations of the pairwise normalized spatial discrepancies between 10 independent reconstructions. The % overlap score gives the overlap as defined by Walther *et al.* (2000) between the averaged and filtered bead models and corresponding PDB structures.

	$tRNA^{Phe}$	24 bp DNA	P4P6 domain
PDB code	1TRA	n.a.	1GID
R_g (experiment)	23.5 ± 0.5	24.2 ± 0.5	29.7 ± 0.5
R_g (PDB)	23.5	24.4	30.4
R_g (bead models)	23.4 ± 0.1	24.75 ± 0.6	31.7 ± 0.3
⟨NSD⟩ (bead models)	0.58 ± 0.01	0.59 ± 0.02	0.70 ± 0.02
% Overlap (beads-PDB)	77.6	81.0	88.4

and overlap scores (see Table 1) identical, within errors, to those generated from data without added noise.

The reconstructed density of the 24 bp DNA duplex is shown in Fig. 4. The cylindrical shape, diameter and length of the duplex get reproduced well, and the periodicity of the major and minor grooves are visible in the reconstruction.

For P4P6 the overall shape and size get again reasonably reproduced. The double stranded protrusion corresponding to P6b (shown on the bottom of Fig. 6) is reconstructed, however, slightly shifted toward the center axis of the molecule. Generally, the reconstructed densities reproduce the size and overall shape of the test molecules faithfully, but are unable to reconstruct details such as specific packing interactions or single stranded protrusions.

3.2. Ion binding PB calculations

We compute the number of excess Mg^{2+} ions bound to $tRNA^{Phe}$ from PB calculations (Fig. 7). Remarkably, the predictions obtained from PB theory using the atomic coordinates and partial charges assigned according to the CHARMM parameter set (thin, solid lines in Fig. 7) agree very well with the values obtained from calculations using the bead reconstructions with uniformly assigned charges to define the molecular geometry (thick, dashed lines). The agreement with the experiment is good for the Rialdi *et al.* (1972) data (Fig. 7, left). For the Römer & Hach (1975) data (Fig. 7, right), the PB predictions tend to fall below the measured values, however, the

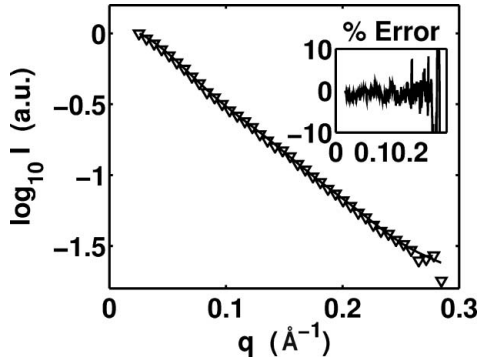

Figure 3
SAXS profiles for the 24 bp DNA duplex. Experimental profile (main graph, triangles) and scattering profile of a representative bead reconstruction (main graph, solid line). The inset shows the relative error $[I_{exp}(q) - I_{beads}(q)]/I_{exp}(q) \times 100\%$.

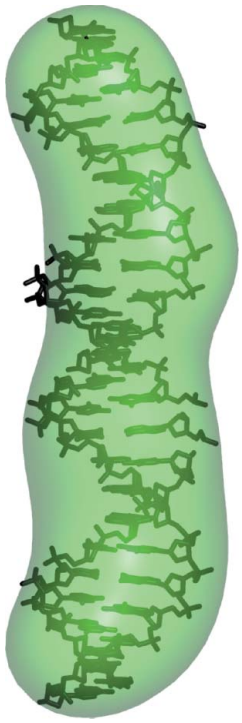

Figure 4
Atomic resolution structure of the 24 bp DNA duplex (rendered as black sticks) and reconstructed density (green transparent surface).

agreement is still reasonable. Possible explanations for the observed deviations are discussed below.

We have used AES experiments to measure the excess number of Na^+, Mg^{2+} and Cl^- ions bound to a 24 bp DNA duplex as a function of $MgCl_2$ against a 20 m*M* NaCl background (Fig. 8, symbols) (Bai *et al.*, 2007). The excess number of Cl^- ions (Fig. 8, triangles) is negative, *i.e.* the co-ion Cl^- is depleted around the DNA with respect to its bulk concentration. The theoretical predictions obtained from PB calculations using the high-resolution structures (Fig. 8, thin, sold lines) agree well with predictions using the reconstructed bead model to define the molecular geometry (thick, dashed lines). The overall agreement with the experimental data is good, however, the PB calculations (in particular those for the all atom model) slightly under-predict the number of Mg^{2+} ions bound (Fig. 8, circles) and over-predict the number of bound Na^+ ions (Fig. 8, squares).

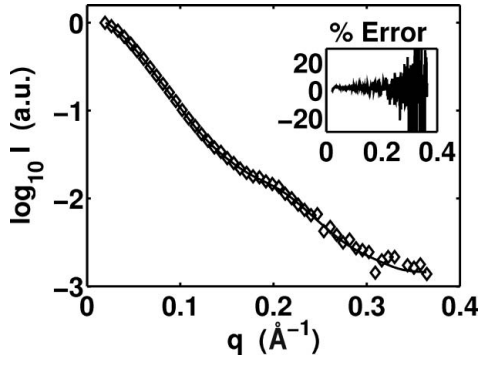

Figure 5
SAXS profiles for the P4P6 domain of the *Tetrahymena* group I intron. Experimental profile (main graph, diamonds) and scattering profile of a representative bead reconstruction (main graph, solid line). $[I_{exp}(q) - I_{beads}(q)]/I_{exp}(q) \times 100\%$.

Figure 6
Atomic resolution structure of the P4P6 domain of the *Tetrahymena* group I intron (rendered as black sticks) and reconstructed density (blue transparent surface).

Das *et al.* (2005) obtain the number of bound excess Mg^{2+} ions as a function of $MgCl_2$ concentration in a 2 *M* NaCl background for wild-type P4P6 and for a mutant that does not bind Mg^{2+} to the 'ion core'. As the two specific 'ion core' Mg^{2+} binding sites are in the interior of the molecules, our PB calculations (which exclude ions from the interior of the molecule) are not expected to capture their contribution to the overall ion binding. We therefore compare the PB simulations with the ion binding data obtained for the P4P6 mutant that does not exhibit specific ion binding to the 'ion core'. This approach neglects small, but measurable, differences between the mutant and wild-type P4P6 solution structures in high-salt concen-

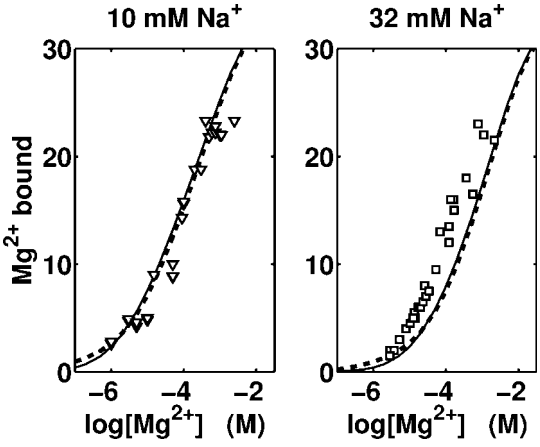

Figure 7
Mg^{2+} ion binding to $tRNA^{Phe}$. Data in 10 m*M* Na^+ background (left, triangles) are taken from Rialdi *et al.* (1972), data in 32 m*M* Na^+ background (right, squares) are from Römer & Hach (1975). Theoretical predictions were obtained from PB calculations using the PDB coordinates (thin, solid lines) or the reconstructed bead model with uniformly assigned charges (thick, dashed lines).

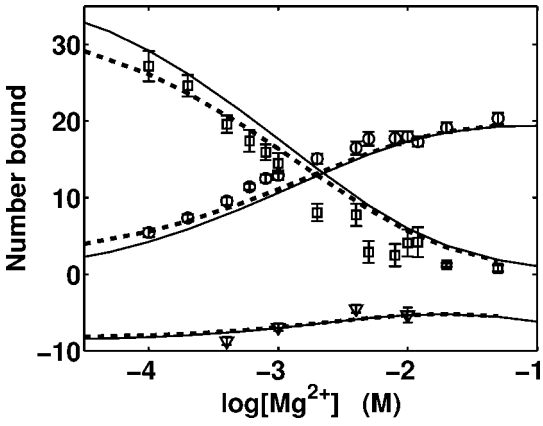

Figure 8
Ion binding to the 24 bp DNA duplex. The number of excess Na^+ (squares) and Mg^{2+} (circles) ions and depleted Cl^- ions (triangles) per DNA was measured by AES (see Materials and methods) as a function of $MgCl_2$ concentration in 20 m*M* NaCl background. Theoretical predictions were obtained from PB calculations using the PDB coordinates (thin, solid lines) or the reconstructed bead model with uniformly assigned charges (thick, dashed lines).

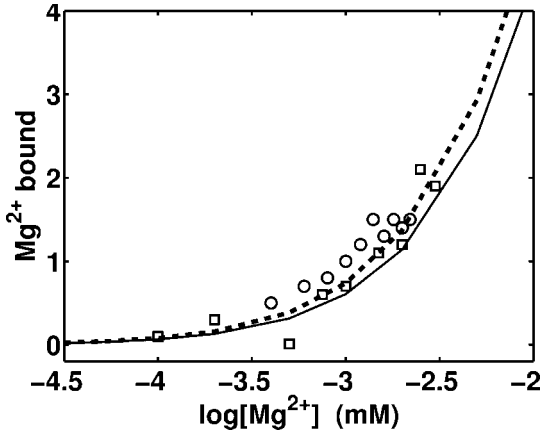

Figure 9
Ion binding to a P4P6 mutant that does not exhibit specific Mg^{2+} binding in the 'ion core'. The number of excess Mg^{2+} ions was measured using a fluorescence indicator (circles) and AES (squares) by Das *et al.* (2005) in 2 *M* NaCl background. Theoretical predictions were obtained from PB calculations using the PDB coordinates (thin, solid lines) or the reconstructed bead model with uniformly assigned charges (thick, dashed lines).

trations (Takamoto *et al.*, 2004). The theoretical predictions using the reconstructed bead model (Fig. 9, thick, dashed line) agree reasonably well with the PB calculations for the atomic resolution coordinates (Fig. 9, thin, solid line). They slightly under-predict the excess number of Mg^{2+} ions determined experimentally, in particular those obtained using the fluorescence indicator HQS (Fig. 9, circles). Overall the agreement with the experiment is remarkable however, given the fact that the data were obtained in 2 *M* NaCl background and that PB theory is generally expected to be valid only in the low concentration limit.

4. Conclusion

We have demonstrated that the bead reconstruction algorithm *DAMMIN* can be used to obtain low-resolution three-dimensional density maps of nucleic acids from SAXS data. Independent reconstruction runs for the same scattering profile yield structurally similar results and the overall shape and geometry of the molecule get well reproduced.

The number of bound excess ions computed from PB calculations using the reconstructed bead models agrees well with the results of calculations using the atomic coordinates. The agreement is remarkable considering that the bead models with uniformly distributed charges only approximate the overall shape and charge distribution of the molecule and ignore considerable molecular details. This might be a consequence of the long-range character of electrostatic interactions. However, it remains to be seen whether a similar level of agreement can also be achieved with regard to other quantities accessible from electrostatic calculations, such as free energies. The PB calculations generally agree well with the experimentally determined ion binding results. However, the theoretical predictions tend to slightly underestimate the number of excess Mg^{2+} ions and over-predict the number of bound Na^+ ions. This is likely owing to ion–ion correlation effects, which are neglected in PB theory. Correlations are expected to be more prominent with divalent ions and to stabilize their binding relative to monovalent ions.

We thank Rhiju Das for providing the P4P6 scattering data and for useful discussions, and Sönke Seifert for help with data collection at the Advanced Photon Source (APS). This research was supported by the National Science Foundation Grant PHY-0140140, and the National Institutes of Health Grant PO1 GM0066275. Use of the APS was supported by the US Department of Energy, Office of Science, Office of Basic Energy Sciences, under Contract No. W-31-109-Eng-38.

References

Bai, Y., Das, R., Millett, I. S., Herschlag, D. & Doniach, S. (2005). *Proc. Natl Acad. Sci. USA*, **102**, 1035–1040.
Bai, Y., Travers, K., Chu, V. C., Lipfert, J., Doniach, S. & Herschlag, D. (2007). Journal, *Submitted - update please.*
Baker, N. A., Sept, D., Joseph, S., Holst, M. J. & McCammon, J. A. (2001). *Proc. Natl Acad. Sci. USA*, **98**, 10037–10041.
Cate, J. H., Gooding, A. R., Podell, E., Zhou, K., Golden, B., Kundrot, C. E., Cech, T. R. & Doudna, J. A. (1996). *Science*, **273**, 1678–1685.
Chacón, P., Morán, F., Díaz, J. F., Pantos, E. & Andreu, J. M. (1998). *Biophys. J.* **74**, 2760–2775.
Das, R., Kwok, L. W., Millet, I. S., Bai, Y., Mills, T., Jacob, J., Maskel, G., Seifert, S., Simon, M., Thiyagarajan, P., Doniach, S., Pollack, L. & Herschlag, D. (2003). *J. Mol. Biol.* **332**, 311–319.
Das, R., Travers, K. J., Bai, Y. & Herschlag, D. (2005). *J. Am. Chem. Soc.* **127**, 8272–8273.
DeLano, W. L. (2002). *The PyMOL Molecular Graphics System*. DeLano Scientific, San Carlos, CA, USA.
Doniach, S. (2001). *Chem. Rev.* **101**, 1763–1778.
Draper, D. E., Grilley, D. & Soto, A. M. (2005). *Ann. Rev. Biophys. Biomol. Struct.* **34**, 221–243.
Fang, X.-W., Golden, B. L., Littrell, K., Shelton, V., Thiyagarajan, P., Pan, T. & Sosnick, T. R. (2001). *Proc. Natl Acad. Sci. USA*, **98**, 4355–4360.
Fang, X.-W., Littrell, K., Yang, X., Henderson, S. J., Seifert, S., Thiyagarajan, P., Pan, T. & Sosnick, T. R. (2000). *Biochemistry*, **39**, 11107–11113.
Gesteland, R. F., Cech, T. & Atkins, J. F. (2006). *The RNA World*. Cold Spring Harbor: Cold Spring Harbor Laboratory Press.
Guinier, A. (1939). *Ann. Phys. (Paris)*, **12**, 161–237.
Kozin, M. B. & Svergun, D. I. (2001). *J. Appl. Cryst.* **34**, 33–41.
Lipfert, J., Millett, I. S., Seifert, S. & Doniach, S. (2006). *Rev. Sci. Inst.* **77**, 461081–461084.
MacKerell, A. D. Jr (1998). *The Encyclopedia of Computational Chemistry*, Vol. 1, pp. 271–277. Chichester: John Wiley & Sons.
Mandal, M. & Breaker, R. R. (2004). *Nature Rev. Mol. Cell. Biol.* **5**, 451–463.
Misra, V. K. & Draper, D. E. (1999). *J. Mol. Biol.* **294**, 1135–1147.
Misra, V. K. & Draper, D. E. (2000). *J. Mol. Biol.* **299**, 813–825.

Rialdi, G., Levy, J. & Biltonen, R. (1972). *Biochemistry*, **11**, 2472–2479.
Römer, R. & Hach, R. (1975). *Eur. J. Biochem.* **55**, 271–284.
Russell, R., Millett, I. S., Doniach, S. & Herschlag, D. (2000). *Nature Struct. Biol.* **7**, 367–370.
Russell, R., Millett, I. S., Tate, M. W., Kwok, L. W., Nakatani, B., Gruner, S. M., Mochrie, S. G. J., Pande, V., Doniach, S., Herschlag, D. & Pollack, L. (2002). *Proc. Natl. Acad. Sci. USA*, **99**, 4266–4271.
Svergun, D. I. (1999). *Biophys. J.* **76**, 2879–2886.
Svergun, D. I., Barberato, C. & Koch, M. H. J. (1995). *J. Appl. Cryst.* **28**, 768–773.
Svergun, D. I. & Koch, M. H. J. (2003). *Rep. Prog. Phys.* **66**, 1735–1782.
Svergun, D. I., Petoukhov, M. V. & Koch, M. H. (2001). *Biophys. J.* **80**(6), 2946–2953.
Takamoto, K., Das, R., He, Q., Doniach, S., Brenowitz, M., Herschlag, D. & Chance, M. R. (2004). *J. Mol. Biol.* **343**, 1195–1206.
Volkov, V. V. & Svergun, D. I. (2003). *J. Appl. Cryst.* **36**, 860–864.
Walther, D., Cohen, F. E. & Doniach, S. (2000). *J. Appl. Cryst.* **33**, 350–363.
Westhof, E. & Sundaralingham, M. (1986). *Biochemistry*, **25**, 4868–4878.
Woodson, S. A. (2005). *Curr. Opin. Chem. Biol.* **9**, 104–109.
Wriggers, W. & Chacón, P. (2001). *J. Appl. Cryst.* **34**, 773–776.
Wriggers, W., Milligan, R. A. & McCammon, J. A. (1999). *J. Struct. Biol.* **125**, 185–195.